RSC Advances

PAPER

View Article Online
View Journal | View Issue

Cite this: *RSC Adv.*, 2026, **16**, 24370

Syngas-derived hydrophilic nanocarbons for water purification

Boborahimov Azamat Boborahim Ugli, [ab] Takeshi Fujita, [c] Shusaku Shoji, [a] Kako Tetsuya*[a] and Hideki Abe *[ab]

Received 13th January 2026
Accepted 14th April 2026

DOI: 10.1039/d6ra00312e

rsc.li/rsc-advances

Fibrous hydrophilic nanocarbon (HNC) materials were synthesized *via* the catalytic reaction of a gas mixture of carbon monoxide (CO) and hydrogen (H_2), *i.e.*, syngas. The synthesized HNC features high specific surface areas and strong adsorption capabilities, rendering it effective for water purification. The HNC surface consists of graphite edge planes functionalized with phenolic hydroxyl groups through interactions with a synthetic byproduct, H_2O vapor. The expanded interlayer spacing of the functionalized edge planes offers an open framework rich in adsorption sites for water-soluble chemical species. Adsorption tests with aqueous dye solutions and actual wastewater demonstrated that HNC outperforms conventional activated carbon, owing to the ability to form strong hydrogen bonds between surface phenolic groups and contaminants.

Introduction

Due to population growth, industrialization, and the rapid expansion of agriculture, water resources are steadily declining.[1,2] Considerable efforts have focused on developing innovative technologies and materials to improve drinking water quality, particularly in emerging countries and densely populated urban areas.[3] Large-scale wastewater treatment plants based on bio-fermentation require substantial capital investment and extensive infrastructure.[4] Although porous ceramics such as zeolites are recognized as effective adsorbent materials for water purification, their high material costs and weight limit large-scale applications.[5] Carbon nanomaterials have attracted significant attention due to their high surface area, low density, and low cost, rendering them suitable for removing a wide range of pollutants, including pharmaceutical residues and volatile organic compounds (VOCs).[6–8]

Expanding the use of nanocarbon materials to wastewater treatment is highly desirable yet remains a significant challenge. Most nanocarbon materials possess inherently lipophilic surfaces, whereas wastewater typically contains hydrophilic substances such as spent detergents and biodegraded organic matter derived from plants and food sources.[9–11] In particular, carbon nanotubes (CNT) and fullerene exhibit lipophilic properties because the surface of these nanocarbon materials consists of the strongly lipophilic basal plane of graphite.[12–14] This lipophilic–hydrophilic mismatch limits the adsorption efficiency and applicability of conventional nanocarbon materials to wastewater. Although post-treatment methods such as steaming, acid treatment, oxidation, and plasma modification can convert carbon nanomaterials hydrophilic, these processes are environmentally unfriendly and costly: they generate large amounts of waste, require strong chemicals, and consume high energy.[15–19]

Here we report that hydrophilic nanocarbon materials can be produced from a gas mixture consisting of carbon monoxide (CO) and hydrogen (H_2), namely syngas, without additional posttreatments. Syngas, readily obtained from industrial processes such as coal gasification, natural gas reforming, and biomass conversion, provides a practical and scalable feedstock.[20–22] Magnetite (Fe_3O_4) nanoparticles serve as a highly effective catalyst, yielding HNC with high purity and well-defined morphology. CO decomposes over the catalyst to produce solid carbon, while H_2 removes oxygen from CO to generate H_2O vapor, imparting hydrophilic functionality to the HNC surface. Experimental results demonstrate that HNC efficiently removes water-soluble contaminants, such as dye molecules, *via* strong hydrogen bonding between surface phenolic hydroxyl groups and the contaminant molecules. The successful direct synthesis of HNC materials from syngas opens avenues for diverse applications beyond water purification, including as conductivity enhancers in battery electrodes consisting of hydrophilic oxides.

Experimental

Catalysts for the synthesis of HNC were prepared using magnetite (Fe_3O_4, Kojundo Kagaku Co.) nanopowder and

[a]*National Institute for Materials Science, Namiki 1-1, Tsukuba, Ibaraki 305-00443, Japan. E-mail: ABE.Hideki@nims.go.jp*

[b]*Graduate School of Science and Engineering, Saitama University, Shimo-Okubo 255, Saitama 338-8570, Japan*

[c]*Kochi University of Technology, Tosayama – Cho, Kami – City, Kochi 782 – 8502, Japan*

carbon black nanopowder (Denka Li 400). Aliquots of 2 g of Fe_3O_4 and 8 g of carbon nanopowders were thoroughly mixed in a mortar. An aliquot of 20 mL of acetone was added and mixed further to obtain thick slurry. Cylindrical catalyst grains with an average diameter of 1 mm and a length of 2 mm were prepared from the slurry using a mincer. The catalyst grains were left dried at room temperature for 24 hours. AB is hydrophobic and poorly disperses in water, whereas acetone wets carbon effectively, improving dispersion. The high volatility of acetone ensures rapid evaporation without residue, enabling uniform and easy drying. The cylindrical catalyst geometry provides extended diffusion paths for CO and H_2, promoting high overall conversion.[23,24]

HNC materials were synthesized over the prepared catalyst in a stream of syngas. An aliquot of 0.5 g of catalyst grains was placed in a tubular furnace. The tubular furnace was first purged with pure argon (Ar) gas for one hour while raising the furnace temperature up to 500 °C. Syngas ($CO : H_2 = 2000 : 200$ mL min^{-1}, respectively) was introduced into the furnace immediately after Ar purging. HNC accumulated on the catalyst grains, yielding 9.7 g after one hour of syngas treatment.

The synthesized HNC was characterized with different techniques. Powder X-ray Diffraction (*p*XRD, PANalytical X'Pert Pro; (Cu Ka, 45 kV, 30 mA)) over a 2θ range of 0° to 90°) was conducted to reveal the structural nature of the material. Purity of the HNC material was evaluated by thermogravimetric/differential thermal analysis (DTG-60H, Shimadzu Corp. Japan). Scanning electron microscopy (SEM, SU8230, Hitachi Corp. Japan) was employed for morphological analysis. Transmission electron microscopy (TEM, JEM-ARM200F NEOARM JEOL) provided insights into the chemical composition and nanostructure of HNC. Porous properties such as specific surface area, pore volume, and pore size were obtained from N_2 adsorption–desorption isotherms at 77 K using a micropore distribution analyser in a relative pressure range between 0.001 and 1 (BELSORP MINI II).

Adsorption performance tests for water-soluble contaminants were conducted using model dyes: Rhodamine B (Merck), Eosin Y (Merck), Rhodamine 123 (Merck), and Rhodamine 6G (Merck) in aqueous solutions. Stock solutions of each dye at 400 mg L^{-1} were prepared, and then diluted by factors of 10, 5, and 2.5, yielding solutions of 40 mg L^{-1}, 80 mg L^{-1}, and 160 mg L^{-1}, respectively. To each 10 mL of the dye solution, 20 mg of HNC was added and stirred using a stirrer for 2, 4, 6, 8, and 60 minutes. After stirring, HNC was removed by filtration through a syringe filter, and the resulting supernatant was transferred into a quartz cell for UV/Vis spectroscopic analysis (wavelength range: 200–850 nm) using a UV/Vis spectrometer (UV-2600, Shimadzu. Japan). The purification performance of HNC for real domestic wastewater was evaluated using actual wastewater. An aliquot of 10 mL of the wastewater was treated with 2, 5, 10 and 20 mg of HNC or an equal amount of activated carbon (AC) (Active Carbon Beads-M 1050-22150, GL Sciences). The wastewater was stirred with a spin bar, filtered, and the resulting supernatants were analysed by UV/Vis spectroscopy to quantify the concentration of visible contaminants such as biodegraded organic materials (UV-2600, Shimadzu. Japan). Fluorescence excitation–emission matrix spectra was further conducted, using a spectrofluorometer (FP-8550, Jasco, Japan), for fluorescent contaminants such as spent detergents.

Results and discussions

Fig. 1a presents the *p*XRD profiles of various carbon materials: Graphite Plate (GP, Nilaco), HNC, Acetylene Black (AB, Denka Li 400), Hard Carbon (HC, Kuranode Type 2, Kuraray), and Activated Carbon (AC). The GP profile shows sharp, intense peaks at 26.4°, 44.1°, 44.5°, and 54.2°, corresponding to the (002), (100), (101), and (004) diffraction peaks of highly ordered graphite. HNC exhibits a similar pattern in terms of reflection positions, with the (002), (100), (101), and (004) diffraction peaks observed at 26.5°, 43.4°, 44.3°, and 54.7°, respectively. However, the HNC peaks are broader than those of GP, indicating that HNC consists of small domains of highly ordered graphite. AB and HC show diffraction peaks at slightly lower angles with broader peaks compared to GP or HNC. The average crystal size and the interlayer spacing (d_{002}) were calculated using the Scherrer and Bragg equations based on the (002) diffraction peak at 2θ = 26.5°, respectively.[25–27] The average crystal size and d_{002} for HNC were calculated as 18.5 nm and 0.3365 nm, respectively. These specific values quantitatively support that HNC consists of small, highly ordered graphitic domains.

The (002) diffraction peaks of AB and HC appear at 26.1° and 25.4°, with full widths at half maximum (FWHM) of 0.38° and 0.88°, respectively. AC exhibits a broad and weak (002) reflection at 33.3°, indicating its amorphous nature. Fig. 1b shows the interlayer spacing (*d*-spacing) calculated from the (002) diffraction peaks in Fig. 1a. The *d*-spacing of HNC is 3.365 Å,

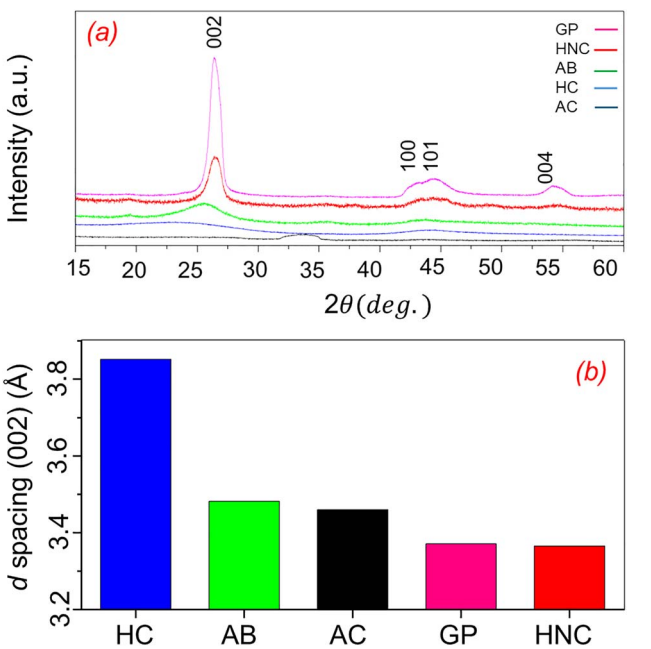

Fig. 1 (a) *p*XRD analysis results of various carbon materials, including Hard Carbon (HC), Activated Carbon (AC), Denka Li 400 (AB), HNC, and Graphite Plate (GP), (b) *d*-spacing values calculated from (002) peaks.

which is close to that of crystalline graphite (3.371 Å). In contrast, AB exhibits a broader interlayer spacing of 3.482 Å, indicative of more disordered layer-to-layer stacking (Fig. 1b). HC shows the largest interlayer spacing of 3.852 Å, characteristic of a highly disordered carbon phase. The reflection peaks of the synthesized HNC are significantly sharper than those of the other carbon materials, highlighting its highly developed atomic ordering.

Thermogravimetric/differential thermal analysis (TG/DTA) was conducted to quantify the carbon content in HNC with a heating temperature from 20 °C to 850 °C under air atmosphere and at a rate of 20 °C min^{-1}. The analysis showed that after heating to 850 °C in air, 2 wt% of incombustible ash remained. Based on this residual mass, the carbon purity of the synthesized HNC material was estimated to be 98 ± 0.5 wt%. (see Fig. S7 for details).

Microscopic analyses by scanning electron microscopy (SEM) and transmission electron microscopy (TEM) were conducted to investigate the morphology of the HNC material. The SEM images demonstrate that HNC possesses a fibrous and twisted morphology (Fig. 2a). TEM observations further showed that each HNC fiber contains a catalyst nanoparticle at one of the ends, which likely served as the growth center of the fiber (Fig. 2b). High-resolution transmission electron microscopy (HRTEM) was carried out to investigate the local structure of HNC. Alternately stacked graphitic basal planes were observed throughout the material (Fig. 2c).

The Fast Fourier Transform (FFT) pattern obtained from the bulk region displayed a paired spots corresponding to the (002*n*) diffraction of the ordered graphitic layers (inset of Fig. 2d). The spacing of the graphitic layers calculated from the FFT pattern was 3.41 Å, which was consistent with the value obtained from *p*XRD, 3.365 Å. In contrast, in the surface region, the interlayer spacing increased to 3.49 Å (inset of Fig. 2e), indicating that the surface of HNC consists of an ordered array of opened graphitic edges that are capable of adopting functional groups. The opened graphitic edges are further functionalized with hydroxyl groups, likely resulting from exposure to water (H_2O) vapor formed through side reactions that accompany the major carbon-deposition pathway, CO disproportionation ($2CO \rightarrow C_{solid} + CO_2$).[28–30] These accompanying reactions include the Bosch reaction ($CO + H_2 \rightarrow H_2O + C_{solid}$) and the reverse water–gas shift reaction ($CO_2 + H_2 \rightarrow H_2O + CO$).[31,32] The Boehm titration analysis confirmed that the functionalized HNC material exhibits a total acidity of 0.04 mmol g^{-1}, attributable to phenolic hydroxyl groups (see SI for details).[33]

The surface chemistry of HNC is governed by phenolic functionalities, which play a significant role in the adsorption performance. Fig. 3a presents the N_2 adsorption–desorption isotherms of HNC as functions of relative pressure. At low relative pressures (p/p_0 = 0.01–0.1), monolayer adsorption predominates, followed by multilayer adsorption in the intermediate range.[34,35] A steep rise in the adsorption volume at higher relative pressures (p/p_0 = 0.1–1) indicates capillary condensation. This adsorption–desorption trend corresponds to a typical Type IV isotherm with a hysteresis loop, characteristic of a mesoporous structure containing microporosity.[36,37]

The pore size distribution, derived from the desorption profile of the isotherm using the Barrett–Joyner–Holanda (BJH) method (Fig. 3b), reveals a primary mesopore population at 2–4 nm.[38] A broader distribution up to 60 nm suggests the presence of larger, secondary mesopores. The average pore diameter was estimated as 21 nm, reflecting a hierarchical porous

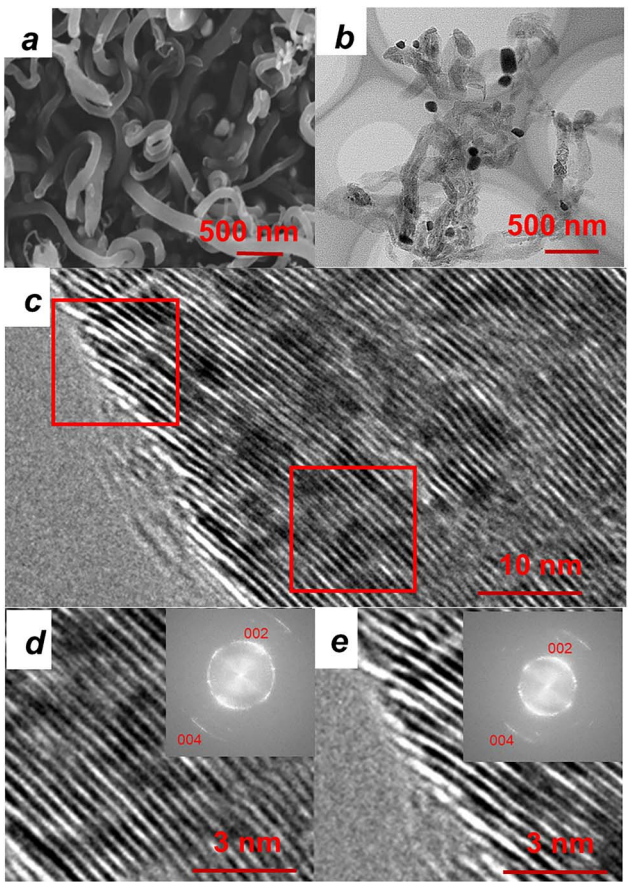

Fig. 2 SEM and TEM micrographs of the HNC materials. (a) Presents SEM images showing variations in surface morphology and pore structure. (b)–(e) Depict TEM images illustrating internal structure, porosity, and nano structural changes. Inset: FFT pattern with reflections corresponding to (002) and (004) graphitic planes.

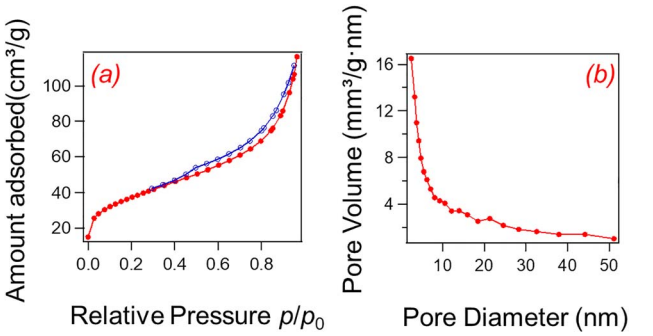

Fig. 3 (a) Nitrogen adsorption–desorption isotherm and (b) BJH pore size distribution.

network of the entangled nanofibers of HNC. This nanonetwork can promote molecular diffusion, rendering the material suitable for transport applications such as molecular and/or sensing. The total pore volume and specific surface area, determined by the BET calculated as 10 $cm^3\ g^{-1}$ and 128 $m^2\ g^{-1}$, respectively.

The dye adsorption performance of the HNC was evaluated under different contact times and initial dye concentrations to investigate the kinetic and isothermal characteristics, respectively (Fig. 4). The adsorption trend was first validated by UV-Vis spectroscopy on four dye solutions (RhB, Rh6G, Rh123, and Eosin Y) each at an initial concentration of 40 mg L^{-1}. Adsorption capacity was evaluated at time intervals of 2, 4, 6, and 8 minutes. As shown in Fig. 4a, the intensity of the RhB absorption peak at 555 nm decreased with increasing time, corresponding to 98% removal after 2 minutes and full decolorization within 8 minutes. Inset shows the colour of the dye solution before and after HNC treatment, demonstrating the high adsorption performance of HNC for RhB.

Fig. 4b illustrates that both RhB and Eosin Y were rapidly adsorbed by the HNC material, achieving maximum removal within 2–4 minutes. In contrast, Rh6G and Rh123 exhibited slower adsorption trends, with capacities increasing from 11.6 to 16.7 mg g^{-1} and 11.6 to 12.7 mg g^{-1}, respectively, over 8 minutes. RhB and Eosin Y demonstrated nearly 100% removal within 8 minutes, indicating strong interactions between the dye molecules and the HNC surface. In contrast, Rh6G and Rh123 showed lower adsorption efficiencies (<64% after 8 minutes), suggesting weaker interactions with the HNC surface.

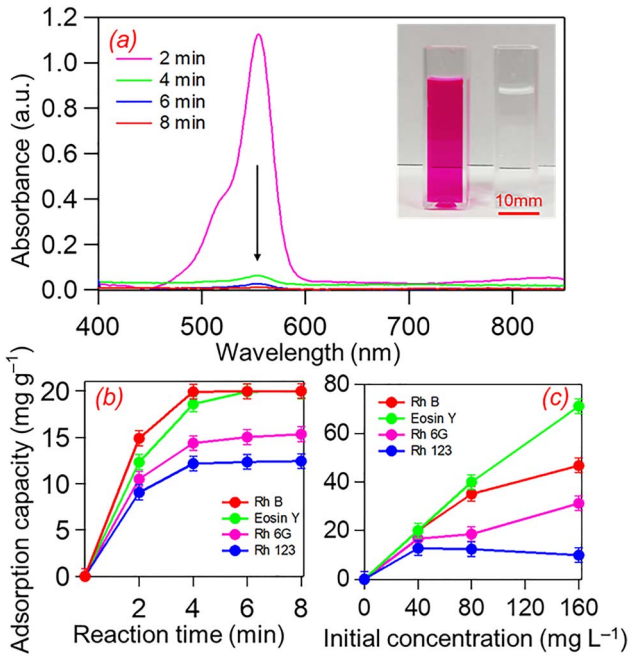

Fig. 4 (a) Evolution of RhB adsorption on HNC at different time intervals, inset: left—RhB (40 mg L^{-1}) before treatment; right—RhB after 8 minutes treatment. (b) Shows adsorption over time, while (c) shows adsorption at different dye concentrations. Error range between 1% and 2%.

The adsorption trend of the four dyes was further investigated at different initial concentrations (40, 80, and 160 mg L^{-1}; Fig. 4c). The adsorption capacity was determined after a 60-minutes contact time. The adsorption capacity of Eosin Y increased from 20.0 mg g^{-1} at 40 mg L^{-1} to 71.1 mg g^{-1} at 160 mg L^{-1}, reflecting the abundance of accessible adsorption sites on the HNC surface. A similar trend was observed for RhB, which reached maximum adsorption capacities of 46.8 mg g^{-1} and 35.5 mg g^{-1}, respectively, at the highest dye concentrations. In contrast, Rh6G and Rh123 exhibited lower adsorption capacities than RhB or Eosin Y as the concentration increased, possibly due to surface saturation or competitive adsorption sites. Table S6 compares our study with the published literature, and it is clear that HNC exhibits high or similar adsorption efficiency compared to other adsorbents reported in the literature.

The zero charge point (pH_{PZC}) is the point at which the net charge on the surface of the photocatalyst is zero or neutral. It was determined using the widely used drift method.[39,40] In this method, 0.01 mol L^{-1} NaCl was prepared, and its initial value was adjusted from 2.29 to 11.16 by adding 0.1 M NaOH or 0.1 M HCl. 20 mg of sample was added to 20 mL solution in a 50 mL beaker, stirred for 24 hours, filtered, and then the final pH of the solution (pH final) was recorded and plotted against the initial pH (pH initial). The point where the graph curve intersected the *x*-axis was taken as the pH_{PZC} value of the sample. The adsorbent surface is positively charged when pH < pH_{PZC} and negatively charged when pH > pH_{PZC}, *i.e.* the surface charge favors the adsorption of F^- ions (electrostatic attraction below pH_{PZC}, repulsion above). In this research, the pH_{PZC} value of the nanocomposite was found to be 6 (see the point of zero charge (pH_{PZC}) in SI, Fig. S10). This value indicates that the HNC produced have acidic character. A similar phenomenon was reported by Ngakou *et al.*[41] and Mesele *et al.*,[39] in which the presence of acidic functional groups on the surface could confer significant cation exchange capacity to the adsorbents. (METTLER TOLEDO SEVENCOMPACT PH/ION S220).

To study the effect of solution pH on dye removal efficiency, the solution pH was changed from 2.7 to 10.5 by adding 0.1 M NaOH or 0.1 M HCl solutions, while the dye concentration was kept constant at 40 mg L^{-1}. Then, 0.02 g of HNC was added and stirred at room temperature for the optimal time. The results showed that when the pH increased from 4.63 to 10.5, the dye removal efficiency decreased from (98 to 87) % after 2 min of contact time (see in SI in table S6 and Fig. S11). In fact, the amount of dye adsorbed on the surface of the adsorbent is affected by the surface charge and, consequently, the pH of the solution.[42]

The reusability of HNC was evaluated by sequential adsorption–desorption cycles using RhB as a model pollutant. After each adsorption cycle, HNC was recovered by filtration and then desorbed using ethanol with mild stirring. The adsorbent was then thoroughly washed with deionized water, dried at 80 °C, and reused for up to three cycles under the same conditions. 20 mg of HNC was stirred with 40 mg L^{-1} of RhB at room temperature for 8 minutes. The residual RhB concentration was recorded for each cycle, and the regeneration efficiency was

calculated based on the initial adsorption capacity. HNC adsorbed 100% of the RhB solution in the first cycle and exhibited 85% and 63% adsorption in the second and third cycles, respectively (see Fig. S12 in the SI). This decrease is partly due to the blocking of pores or the irreversible binding of RhB molecules to high-affinity sites that are not easily desorbed under mild conditions.

Fig. 5a presents structural models of the dyes. All four dyes share a common xanthene–benzene moiety but differ in their functional groups. RhB and Eosin Y contain carboxyl groups directly attached to the benzene ring, whereas Rh123 and Rh6G have ether-terminated groups instead. Consequently, both RhB and Eosin Y are able to form strong hydrogen bonds with the phenolic hydroxyl groups on the HNC surface, whereas neither Rh123 nor Rh6G (Fig. 5b).[43]

Adsorption of RhB and Eosin Y is further enhanced by π–π interactions between the planar xanthene moiety and the honeycomb carbon surface.[44–46] Rh123 and Rh6G rely solely on π–π interactions, resulting in slower adsorption kinetics and lower saturation capacities (Fig. 5c).

Eosin Y exhibited higher adsorption at saturation than RhB: at an initial dye concentration of 160 mg L^{-1}, RhB reaches 40 mg g^{-1}, while Eosin Y continues to increase toward 80 mg g^{-1} (Fig. 4c). This result suggests a greater number of accessible adsorption sites for Eosin Y. The adsorption of RhB (40 mg g^{-1} ≈ 0.08 mmol per gram of HNC) corresponds to twice the amount of phenolic hydroxyl groups in HNC (0.04 mmol g^{-1}), indicating hydrogen bonding between one carboxyl group and two phenolic hydroxide groups. Eosin Y, being the smallest molecule with no bulky functional groups attached to the Xanthene moiety (Fig. 5a), can penetrate the open edges of the graphitic basal planes, enabling interactions not only *via* hydrogen bonds but also through π–π interactions.[9,47]

Finally, the purifying performance of the HNC material was evaluated for actual domestic wastewater. Two types of carbon adsorbents were tested: the synthesized HNC and commercially available activated carbon (AC, GL sciences). In each experiment, 10 mL of wastewater was mixed with a fixed amount of the carbon materials and stirred for 2 hours. Fig. 6a shows that the absorbance of HNC-treated wastewater is almost zero in the visible region (≈380 nm), whereas that of AC-treated wastewater remains finite (dose of 2000 mg L^{-1}). These results clearly indicate that HNC is more effective than AC at removing visible contaminants, such as colored organic matter, from wastewater. Moreover, the experiments have demonstrated that HNC is more capable than AC of removing fluorescent chemical species likely from spent detergents. The inset shows a pair of wastewater samples treated with HNC (left) and AC (right),

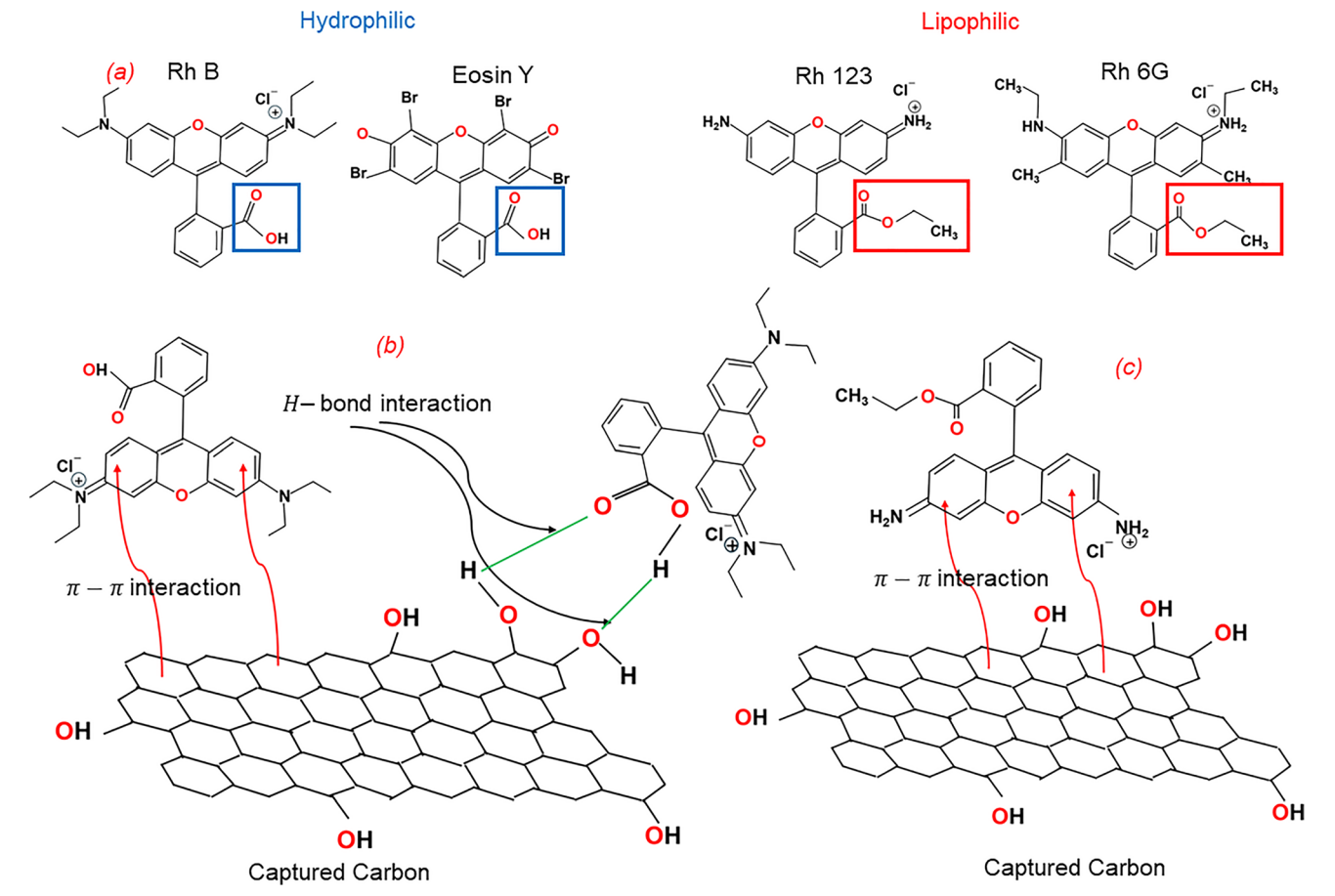

Fig. 5 (a) Molecular structure of the dye molecules, possible interaction between HNC and (b) hydrophilic dyes and (c) lipophilic dyes (green line H-bond interaction; red line π–π interaction).

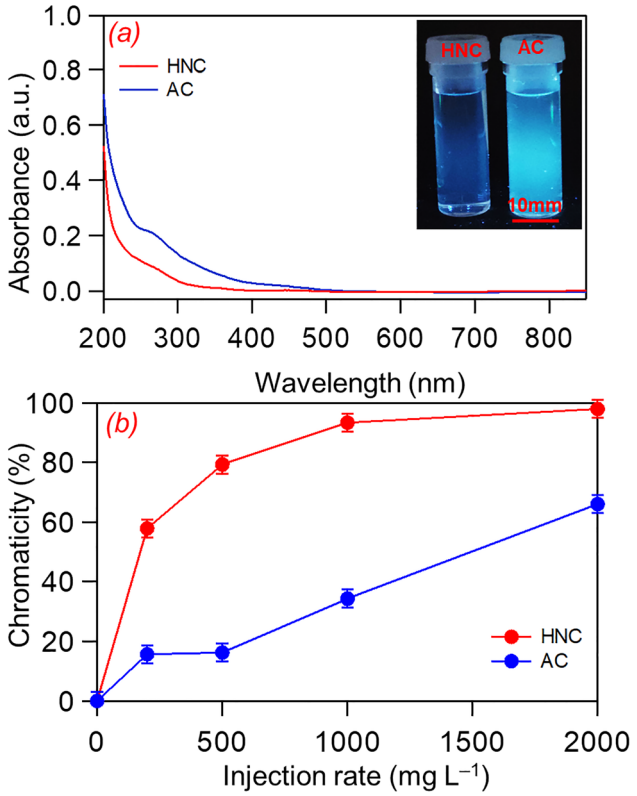

Fig. 6 (a) UV-Vis spectra for actual wastewater after purification with ctivated Carbon (AC) and HNC, (b) chromaticity at a wavelength of 390 nm as a function of the injection rate of carbon adsorbents. Error range between 1% and 2%.

illuminated laterally with UV light (NULED-102CT, 367 nm). The AC-treated wastewater exhibited pale-blue fluorescence, whereas no fluorescence was observed for the HNC-treated sample (see the fluorescence spectra in SI, Fig. S9).

These observations indicate that HNC removes fluorescent chemicals more efficiently than AC, due to its ability to form hydrogen bonds with water-soluble chemical species.

The decolorization performance of HNC was further evaluated by comparing the UV-Vis absorption at the wavelength 390 nm at increasing dosages (200, 500, 1000, and 2000 mg L^{-1}). For AC, the corresponding chromaticity values were 16%, 17%, 35%, and 66%, whereas for HNC, the values were 58%, 80%, 94%, and 98%, respectively (Fig. 6b). These results confirm that HNC is an effective alternative to commercial AC for wastewater treatment (see Fig. S8 for the trend of the decolorization acetylene black material (AB, Denka Li 400)). Table S8 presents the water quality indicators of the actual wastewater in this study.

Conclusion

In conclusion, hydrophilic nanocarbon (HNC) materials were successfully synthesized directly from a CO/H_2 gas mixture (syngas) without post-treatment. Magnetite (Fe_3O_4) nanoparticles acted as highly effective catalysts, producing HNC with a high yield, controlled purity, and well-defined morphology. CO decomposes over the catalyst to deposit solid carbon, while H_2 removes oxygen from CO to generate H_2O vapor, imparting hydrophilic functionality to the HNC surface. The resulting HNC material demonstrated strong adsorption of dyes containing oxyphilic functional groups such as carboxyl groups, through hydrogen bonding with surface phenolic hydroxyl groups. The effectiveness of HNC adsorbate was further validated in water purification tests using real domestic wastewater, confirming its ability to remove water-soluble contaminants. Syngas is produced on a large scale from methane with CO_2 or steam *via* established reforming processes, as well as from waste plastics and biogas. Because HNC is obtained from syngas in relatively high yield, its production cost and energy consumption can be lower than those of conventional nanocarbons such as carbon black derived from petroleum combustion. Given the substantial global trade of methane and CO_2 (on the order of 100 Mt annually), HNC production has the potential to meet the demand for activated carbon in wastewater treatment, which is approximately 1 Mt per year.[48] Beyond water treatment, syngas-derived HNC shows potential for broader applications, including gas adsorption and sensing, electrocatalysis, and as conductivity enhancers in battery electrodes.

Author contributions

Boborahimov Azamat B.·U synthesized and characterized the HNC. Microscopic observations were conducted by T. Fujita, Boborahimov Azamat B.·U, H. Abe, Sh. Shoji, and K. Tetsuya wrote and edited the manuscript. All authors have read and approved the published version of the manuscript.

Conflicts of interest

The authors declare no conflicts of interest.

Data availability

Data for this article, including the original dataset for the water-purification performance tests, are available at ZENODO https://doi.org/10.5281/zenodo.18059466.

Supplementary information (SI) is available. See DOI: https://doi.org/10.1039/d6ra00312e.

Acknowledgements

This work is based on results obtained from a project, JPNP14004, commissioned by the New Energy and Industrial Technology Development Organization (NEDO).

References

1 J.-W. Lee, H.-C. Kang, W.-G. Shim, C. Kim, K.-S. Yang and H. Moon, Heterogeneous adsorption of activated carbon nanofibers synthesized by electrospinning polyacrylonitrile solution, *J. Nanosci. Nanotechnol.*, 2006, **6**, 3577–3582.
2 W. Xiao, Z. N. Garba, S. Sun, I. Lawan, L. Wang, M. Lin and Z. Yuan, Preparation and evaluation of an effective activated

carbon from white sugar for the adsorption of rhodamine B dye, *J. Clean. Prod.*, 2020, **253**, 119989.
3 Y. Si, T. Ren, B. Ding, J. Yu and G. Sun, Synthesis of mesoporous magnetic Fe_3O_4@carbon nanofibers utilizing *in situ* polymerized polybenzoxazine for water purification, *J. Mater. Chem.*, 2012, **22**, 4619–4622.
4 S. Dutta, B. Gupta, S. K. Srivastava and A. K. Gupta, Recent advances on the removal of dyes from wastewater using various adsorbents: A critical review, *Mater. Adv.*, 2021, **2**, 4497–4531.
5 M. M. Sabzehmeidani, S. Mahnaee, M. Ghaedi, H. Heidari and V. A. L. Roy, Carbon based materials: A review of adsorbents for inorganic and organic compounds, *Mater. Adv.*, 2021, **2**, 598–627.
6 Y. El Ouardi, A. El Aissouq, A. Chennah, A. Ouammou and K. Laatikainen, Synthesis, characterization, and DFT investigation of rhodamine B dye removal by activated carbon produced from argan nutshell, *Biomass Convers. Biorefin.*, 2024, **14**, 15107–15118.
7 A. S. Hamda, H. A. Areti, R. L. Gudeta, L. D. Abo and M. Jayakumar, Carbon-based nanomaterials for water treatment: A comprehensive review of recent advances and mechanisms, *Chem. Eng. J. Adv.*, 2025, **23**, 100834.
8 I. Salahshoori, Q. Wang, M. A. L. Nobre, A. H. Mohammadi, E. A. Dawi and H. A. Khonakdar, Molecular simulation-based insights into dye pollutant adsorption: A perspective review, *Adv. Colloid Interface Sci.*, 2024, **333**, 103281.
9 P. K. Malik, Use of activated carbons prepared from sawdust and rice-husk for adsorption of acid dyes: A case study of Acid Yellow 36, *Dyes Pigm.*, 2003, **56**, 239–249.
10 H. Liu and L. Li, Graphitic materials: intrinsic hydrophilicity and its implications, *Extreme Mech. Lett.*, 2017, 44–50.
11 M. Sherief and A. A. Hassan, The impact of wastewater quality and flow characteristics on H_2S emissions generation: statistical correlations and an artificial neural network model, *Water*, 2022, **14**, 791.
12 A. Helland, P. Wick, A. Koehler, K. Schmid and C. Som, Reviewing the environmental and human health knowledge base of carbon nanotubes, *Environ. Health Perspect.*, 2007, **115**, 1125–1131.
13 M. M. Jacobs, M. Ellenbecker, P. Hoppin, D. Kriebel and J. Tickner, Precarious promise: A case study of engineered carbon nanotubes, *Environ. Health Perspect.*, 2010, **118**, 460–464.
14 N. Jayaprakash, K. Elumalai, S. Manickam, G. Bakthavatchalam and P. Tamilselvan, Carbon nanomaterials: Revolutionizing biomedical applications with promising potential, *J. Drug Deliv. Sci. Technol.*, 2022, **75**, 103676.
15 T. Ahamad, M. Naushad, K. Ruksana, A. N. Alhabarah and S. M. Alshehri, N/S doped highly porous magnetic carbon aerogel derived from sugarcane bagasse cellulose for the removal of bisphenol-A, *Int. J. Biol. Macromol.*, 2019, **132**, 1031–1038.
16 H. Z. Wang, Z. P. Huang, Q. J. Cai, K. Kulkarni, C.-L. Chen, D. Carnahan and Z. F. Ren, Reversible transformation of hydrophobicity and hydrophilicity of aligned carbon nanotube arrays and buck papers by dry processes, *Carbon*, 2010, **48**, 868–875.
17 S. Yoo, D. Seok, Y. Jung and K. Lee, Hydrophilic surface treatment of carbon powder using CO_2 plasma activated gas, *Coatings*, 2021, **11**, 925.
18 P. Stelmachowski, D. Maj, G. Grzybek, K. Kruczała and A. Kotarba, Functionalization of graphite with oxidative plasma, *Int. J. Mol. Sci.*, 2022, **23**, 9650.
19 S. Wang, Y. Wang, M. Gao and Y. Huang, Aging effect of plasma-treated carbon fiber surface: from an engineering point, *Coatings*, 2024, **14**, 80.
20 X. Song and Z. Guo, A new process for synthesis gas by co-gasifying coal and natural gas, *Fuel*, 2005, **84**, 525–531.
21 Z. Cao, J. Gao, H. Jin, H. Zhou, M. Cohron, H. Zhao, H. Liu and W. Pan, Synthesis gas production with an adjustable H_2/CO ratio through the coal gasification process: effects of coal ranks and methane addition, *Energy Fuels*, 2008, **22**, 1720–1730.
22 Ö. Tezer, N. Karabağ, A. Öngen, C. Ö. Çolpan and A. Ayol, Biomass gasification for sustainable energy production: a review, *Int. J. Hydrogen Energy*, 2022, **47**, 15419–15433.
23 R. Hubble, A. P. E. York and J. S. Dennis, Modelling reaction and diffusion in a wax-filled hollow cylindrical pellet of Fischer Tropsch catalyst, *Chem. Eng. Sci.*, 2019, 958–969.
24 A. Nanduri and P. L. Mills, Effect of catalyst shape and multicomponent diffusion flux models on intraparticle transport kinetic interactions in the gas-phase Fischer–Tropsch synthesis, *Fuel*, 2020, **278**, 118117.
25 H. M. Albetran, Synthesis and characterization of electrospun carbon nanofibers from polyacrylonitrile and graphite nanoplatelets, *Materials*, 2023, **16**, 1749.
26 H. M. Albetran, Investigation of the morphological, structural, and vibrational behaviour of graphite nanoplatelets, *J. Nanomater.*, 2021, **2021**, 5546509.
27 I.-M. Low, H. M. Albetran and M. Degiorgio, Structural characterization of commercial graphite and graphene materials, *J. Nanotechnol. Nanomater.*, 2020, **1**, 23–30.
28 A. A. Vedyagin, I. V. Mishakov and P. G. Tsyrulnikov, The features of the CO disproportionation reaction over iron-containing catalysts prepared by different methods, Reaction Kinet, *Mech. Catal.*, 2016, **117**, 35–46.
29 H. Nakano, S. Kawakami, T. Fujitani and J. Nakamura, Carbon deposition by disproportionation of CO on a Ni (977) surface, *Surf. Sci.*, 2000, **454–456**, 295–299.
30 J. L. Weber, C. Hernández Mejía, K. P. de Jong and P. E. de Jongh, Recent advances in bifunctional synthesis gas conversion to chemicals and fuels with a comparison to monofunctional processes, *Catal. Sci. Technol.*, 2024, **14**, 4799–4842.
31 R. Becka, S. Bajohr and T. Kolb, Review on CO_2 activation *via* catalytic reverse water–gas shift reaction, *Chem. Ing. Tech.*, 2025, **97**, 860–881.
32 O. S. Mendoza-Hernandez, A. Shima, H. Matsumoto, M. Inoue, T. Abe, Y. Matsuzaki and Y. Sone, Exergy valorization of a water electrolyzer and CO_2 hydrogenation tandem system for hydrogen and methane production, *Sci. Rep.*, 2019, **9**, 6470.

33 J. Hou, L. Xu, Y. Han, Y. Tang, H. Wan, Z. Xu and S. Zheng, Deactivation and regeneration of carbon nanotubes and nitrogen-doped carbon nanotubes in catalytic peroxymonosulfate activation for phenol degradation: variation of surface functionalities, *RSC Adv.*, 2019, **9**, 974–983.

34 K. Markuske, K. Schaldach, T. Storch, K. Khajryan, V. Herdegen and T. Fieback, Technological characterisation of an innovative shaped carbon from bagasse by comparison to two commercially available carbons, *Carbon Trends*, 2025, **21**, 100567.

35 H. He, K. Wang, J. Pan, X. Wang and Z. Wang, Characteristics of coal porosity changes before and after triaxial compression shear deformation under different confining pressures, *ACS Omega*, 2022, **7**, 16728–16739.

36 E. Pérez-Botella, S. Valencia and F. Rey, Zeolites in adsorption processes: state of the art and future prospects, *Chem. Rev.*, 2022, **122**, 17647–17695.

37 I. Cătălin, O. Verdes and M. Suba, Nitrogen sorption measurements and thermal analysis techniques, in *Batteries & Fuel Cells; Applied Microbiology; Solar Energy & Photovoltaics*, 2023, pp. 201–228.

38 J. Villarroel-Rocha, D. Barrera and K. Sapag, Introducing a self-consistent test and the corresponding modification in the Barrett, Joyner and Halenda method for pore-size determination, *Microporous Mesoporous Mater.*, 2014, **200**, 68–78.

39 M. Mengesha, Y. Shuka, T. Eyoel and T. Tesfaye, Novel biomaterial-derived activated carbon from Lippia adoensis (Var. Koseret) leaf for efficient organic pollutant dye removal from water solution, *Am. J. Appl. Chem.*, 2024, **12**, 29–46.

40 M. Mohammadi, A. J. Hassani, A. R. Mohamed and G. D. Najafpour, Removal of Rhodamine B from aqueous solution using palm shell-based activated carbon: adsorption and kinetic studies, *J. Chem. Eng. Data*, 2010, **55**, 5777–5785.

41 N. S. Christian, N. H. Manga, T. T. D. Raoul and A. S. Gabche, Optimisation of activated carbon preparation by chemical activation of Ayous sawdust, Cucurbitaceae peelings and hen egg shells using response surface methodology, *Int. Res. J. Pure Appl. Chem.*, 2017, **14**, 1–12.

42 T. Iida, K. Saito, M. Yamashita and H. Tanaka, Effect of surface property of activated carbon on adsorption of nitrate ion, *Chem. Pharm. Bull.*, 2013, **61**, 1280–1285.

43 H. Ren, D. D. Kulkarni, R. Kodiyath, W. Xu, I. Choi and V. V. Tsukruk, Competitive adsorption of dopamine and rhodamine 6G on the surface of graphene oxide, *ACS Appl. Mater. Interfaces*, 2014, **6**, 2459–2470.

44 S. Jayanthi, N. K. R. Eswara, S. A. Singh, K. Chatterjee, G. Madras and A. K. Sood, Macroporous three-dimensional graphene oxide foams for dye adsorption and antibacterial applications, *RSC Adv.*, 2016, **6**, 1158–1168.

45 R. Vinu, S. U. Akki and G. Madras, Investigation of dye functional group on the photocatalytic degradation of dyes by nano-TiO_2, *J. Hazard. Mater.*, 2010, **176**, 765–773.

46 P. M. Nandanwar, Composite materials for dye capture: a comprehensive review, *J. Phys. Conf. Ser.*, 2025, **3076**, 012017.

47 G. Zhao and H. Zhu, Cation–π interactions in graphene-containing systems for water treatment and beyond, *Adv. Mater.*, 2020, **32**, 1905756.

48 ARPA-E, *Hydrogen Shot Summit: Methane Pyrolysis Panel*, 2021.